Aseismic slip and seismogenic coupling in the Marmara Sea: What can we learn from onland geodesy?

Emilie Klein, Zacharie Duputel, Frédéric Masson, Hakan Yavasoglu, Agram Piyush

AGU PUBLICATIONS

Geophysical Research Letters

RESEARCH LETTER
10.1002/2017GL072777

Key Points:
- We propose a probabilistic interseismic model of the main Marmara Sea fault
- Our Bayesian analysis suggest creep in the central segments with large uncertainties due to the paucity of GPS stations in this area
- We implement a network optimization procedure to identify the most favorable distribution of stations in the Marmara Sea

Supporting Information:
- Supporting Information S1

Correspondence to:
E. Klein,
emilie.klein@unistra.fr

Citation:
Klein, E., Z. Duputel, F. Masson, H. Yavasoglu, and P. Agram (2017), Aseismic slip and seismogenic coupling in the Marmara Sea: What can we learn from onland Geodesy?, *Geophys. Res. Lett.*, *44*, 3100–3108, doi:10.1002/2017GL072777.

Received 23 JAN 2017
Accepted 13 MAR 2017
Accepted article online 21 MAR 2017
Published online 10 APR 2017

Aseismic slip and seismogenic coupling in the Marmara Sea: What can we learn from onland geodesy?

E. Klein[1], Z. Duputel[1], F. Masson[1], H. Yavasoglu[2], and P. Agram[3]

[1]Institut de Physique du Globe; UMR 7516, Université de Strasbourg/EOST CNRS, Strasbourg, France, [2]Geomatics Engineering, ITU, Istanbul, Turkey, [3]Jet Propulsion Laboratory, Pasadena, California, USA

Abstract Ever since the M_w7.4 Izmit earthquake in 1999, evaluation of seismic hazard associated with the last unbroken segments of the North Anatolian fault is capital. A strong controversy remains over whether Marmara fault segments are locked or are releasing strain aseismically. Using a Bayesian approach, we propose a preliminary probabilistic interseismic model constrained by published GPS data sets. The posterior mean model show that Ganos and Cinarcik segments are locked while creep is detected in the central portion of Marmara fault. Our analysis, however, reveals that creeping segments are associated with large model uncertainties, which mainly results from the sparsity of current geodetic observations. We then discuss how the GPS network can be improved to attain more reliable assessment of interseismic slip rates. With this purpose, we implement a network optimization procedure to identify the most favorable distribution of stations measuring strain accumulation in the Marmara Sea.

1. Introduction

Extending over more than 1500 km, the North Anatolian Fault (NAF) is a major continental strike-slip fault running from eastern Turkey up to the Aegean Sea. With a right-lateral geodetic slip rate of about 25 mm/yr, it accommodates the relative motion between the Eurasian and Anatolian plates. In 1999, the $M_w = 7.4$ Izmit and $M_w = 7.1$ Düzce earthquakes ended a westward migrating seismic sequence of eight $M_w > 7$ events that started in 1939 with the $M_w = 7.9$ Erzincan earthquake in eastern Turkey (Figure 1). This sequence is commonly explained by stress transfer triggering [*Stein et al.*, 1997]. Consequently, the segments located in the Marmara Sea, shaping a 70 km to 150 km gap unbroken since 1766 [*Ambraseys*, 2002; *Armijo et al.*, 2005; *Meghraoui et al.*, 2012], have now great odds of being the scene of the next great earthquake. Located offshore Istanbul, a proper estimation of strain accumulation is crucial to evaluate seismic hazard and seismic risk in the Marmara region.

Because they allow precise quantification of surface deformation, geodetic observations such as GPS and interferometric synthetic aperture radar (InSAR) are commonly used to study the behavior of faults during the interseismic period, highlighting two different regimes: locked (fully or partially), therefore accumulating strain likely to be released during large earthquakes or slipping aseismically. The Marmara fault presents the major difficulty of being undersea, preventing any standard geodetic measurements within 10 to 20 km of the fault. This fundamental limitation combined with the poor data coverage in the western Istanbul region clearly complicates the characterization of the Marmara fault behavior. The bathymetry of the Marmara Sea is marked by four basins from which we define four eponymous segments represented on Figure 1b, hereafter TS for Tekirdag, CeS for Central, KS for Kumburgaz, and CiS Cinarcik. Preliminary studies using land-based geodetic measurements suggest a creeping segment encompassing the CeS and KS [*Ergintav et al.*, 2014] in agreement with seismic repeaters identified in the Central basin by *Schmittbuhl et al.* [2016] (Figure 1). The integration of seafloor geodetic data reveals a locally locked zone in the KS [*Sakic et al.*, 2016]. Seismological studies also conclude that this segment is accumulating stress and is mature enough to experience an earthquake of magnitude $M_w \sim 7$ [*Schmittbuhl et al.*, 2015].

In this study, we show that the difficulty of assessing strain accumulation in the Marmara fault results both from the simplicity of current geodetic models and from the scarcity of available geodetic data. We highlight that simple infinite fault model classically used to investigate interseismic deformation cannot be employed in the Marmara Sea. Going forward, we propose a probabilistic interseismic model assuming a more realistic 3-D geometry of the fault. Although our results are consistent with previous studies, slip rate in the central

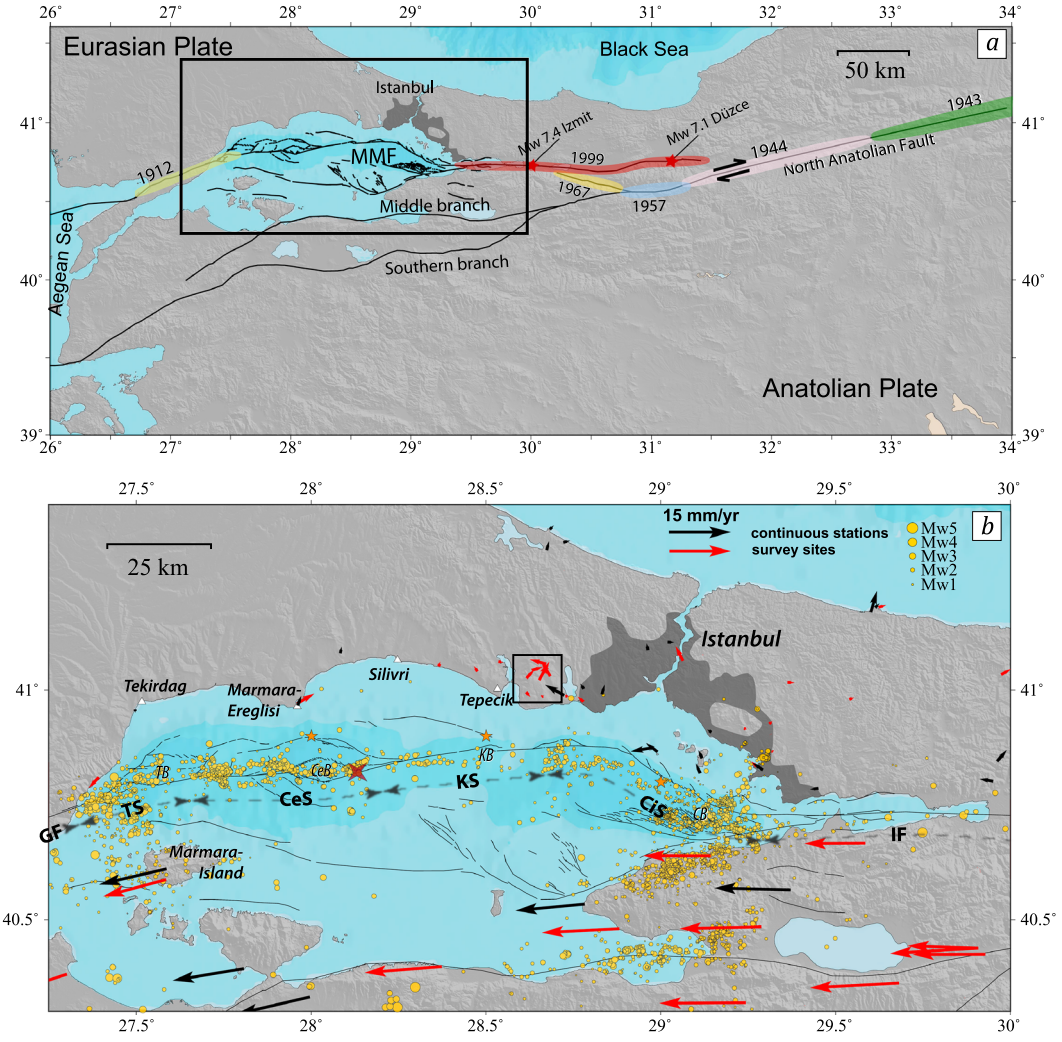

Figure 1. (a) Main ruptures along the NAF. (b) Seismicity between 2007 and 2011 [*Schmittbuhl et al.*, 2015] the red cross depicts the location of repeaters (CeB) [*Schmittbuhl et al.*, 2016] and GPS velocity in the study area [*Ergintav et al.*, 2014]. TS refers to Tekirdag, CeS to Central, KS to Kumburgaz, and CiS to Cinarcik Segments. The eponymous basins are also indicated [*Le Pichon et al.*, 2003]. Orange stars depict the locations of major historical earthquakes [*Ambraseys*, 2002; *Bohnhoff et al.*, 2016].

Marmara fault segments remain uncertain due to sparse GPS measurements in this region. We discuss how the existing observational capability could be improved by designing an optimum GPS network.

2. Strain Accumulation Modeling

2.1. Effect of the 3-D Fault Geometry

For a linear infinite strike-slip fault, surface velocities (v) measured interseismically as function of distance from the fault (x) are given by

$$v(x) = V/\pi \cdot \arctan(x/D) \tag{1}$$

where V is the fault slip rate below the locking depth D [*Savage and Burford*, 1973]. This model is convenient when dealing with simple linear strike-slip faults since it allows the estimation of locking depth and far field plate velocity from displacement profiles. Such 2-D representation of interseismic deformation was used by most previous studies investigating strain accumulation along the Marmara fault [*Ergintav et al.*, 2014; *Diao et al.*, 2016a]. However, in this region, the NAF is nonplanar and features a double fault bend close to Istanbul (cf. Figure 1) [*Le Pichon et al.*, 2001, 2003; *Armijo et al.*, 2005].

To evaluate the impact of this geometry on deformation, we compare the response of a linear infinite strike-slip fault to the one of a more realistic 3-D fault. To design this realistic fault, we use a simplified geometry designed from seismicity, geological and bathymetry data [*Le Pichon et al.*, 2001; *Armijo et al.*, 2005; *Schmittbuhl et al.*, 2015]. We test two simple cases: (1) the faults are freely creeping at a constant rate (Figures S1a and S1b in the supporting information), and (2) the faults are locked down to 15 km depth, corresponding to the average depth of the seismogenic zone estimated from seismicity [*Schmittbuhl et al.*, 2015], below which the fault is slipping at plate rate (Figure S1c). For the infinite strike-slip fault, surface displacements are parallel and symmetrical with respect to the fault trace (as expected). On the contrary, the 3-D fault geometry is associated with a clockwise rotation, visible more than 25 km west of the fault kink in the KS. For both fully creeping and locked faults, this results in asymmetrical velocity profiles that differs from the response of an infinite strike-slip fault.

Beyond geometrical complexities, the fault can also present important along-strike coupling variations. Coupling (or locking) is here defined as the amount of plate rate not released as interseismic creep. Strain modeling along the eastern part of the NAF indicates nonnegligible variations of locking depth and slip rate [e.g., *Tatar et al.*, 2012; *Aktug et al.*, 2015; *Hussain et al.*, 2016]. Such spatial variability of interseismic coupling is visible on other major continental strike-slip faults (e.g., the San Andreas fault) [*Jolivet et al.*, 2015], and locking is often correlated with the location of earthquake ruptures [*Maurer and Johnson*, 2014; *Barbot et al.*, 2013]. In the Marmara Sea, the first months of seafloor acoustic measurements suggest that the KS is coupled and accumulating stress [*Sakic et al.*, 2016]. However, these measurements, made in a very localized area, may not be representative of the entire segment behavior. Further west, *Schmittbuhl et al.* [2016] identified the occurrence of seismic repeaters, which are possible markers of aseismic creep in the CeS.

In the following, we will use a 3-D fault to account for the overall geometry of the Marmara fault and to restore possible spatial variations of interseismic slip rate. Note that, since GPS data is not available within 10 to 20 km of the fault, a highly precise fault geometry is not necessary. According to our tests, a latitudinal shift of the fault location by 1 or 2 km will not affect coupling estimates given GPS measurement uncertainties.

2.2. GPS Data in the Western Istanbul Region

The eastern region of Istanbul is one of the first regions where GPS measurements have been performed in the early 1990s [*Straub et al.*, 1997]. The first stage of the Marmara GPS network (MAGNET) was installed by the TUBITAK Marmara Research Center just before the 1999 Izmit earthquake. Ever since, GPS surveys were intensified along the continental part of the fault and, supported by the increasing quantity of data, numerous studies focused on the quantification of postseismic deformations following the Izmit and Düzce earthquakes [*Ergintav et al.*, 2002; *Bürgmann et al.*, 2002; *Hearn et al.*, 2009]. Even if numerous studies have investigated strain accumulation in the Marmara Sea [*McClusky et al.*, 2000; *Ergintav et al.*, 2014; *Diao et al.*, 2016b], geodetic measurements in the western region of Istanbul remain sparse. Because of difficult field conditions, no systematic coverage have yet been performed along the shoreline of the TS and CeS, and inland, between Marmara and Black seas shorelines (Figure 1b).

In the following section, we use the velocity table published by [*Ergintav et al.*, 2014], having removed about ten sites that are perturbed by nearby landslides (precise list of stations provided Table S1 in the supporting information).

2.3. Bayesian Modeling of Strain Accumulation

We model the GPS velocity field assuming a simplified 3-D fault geometry. The seismogenic zone is discretized using two rows of subfaults ranging from the free surface down to 15 km depth. Interseismic loading (i.e., far-field displacements) is modeled by slip on patches deeper than 15 km extending to infinite depth (effectively 5000 km). Laterally, the fault extends to about 1000 km away from the studied area, following the NAF trace. In addition to slip in each subfault, we also estimate translation, rotation, and scaling parameters to deal with GPS reference frame issues. The forward problem is defined as $\mathbf{d} = \mathbf{Gm}$ where $\mathbf{d}$ is a vector containing the horizontal component of the GPS velocity field, $\mathbf{m}$ a vector containing the model parameters described above, and $\mathbf{G}$ is the Green's function matrix. For simplicity, we assume pure strike-slip faulting and an homogeneous semiinfinite elastic medium [*Okada*, 1985]. We explore the space of possible solutions using a Bayesian approach to derive the posterior probability density function (PDF) of the model $\mathbf{m}$ given available observations $\mathbf{d}_{obs}$:

$$p(\mathbf{m}|\mathbf{d}_{obs}) \propto p(\mathbf{m}) \exp\left(-\frac{1}{2}(\mathbf{d}_{obs} - \mathbf{Gm})^T \mathbf{C}_\chi^{-1} (\mathbf{d}_{obs} - \mathbf{Gm})\right) \quad (2)$$

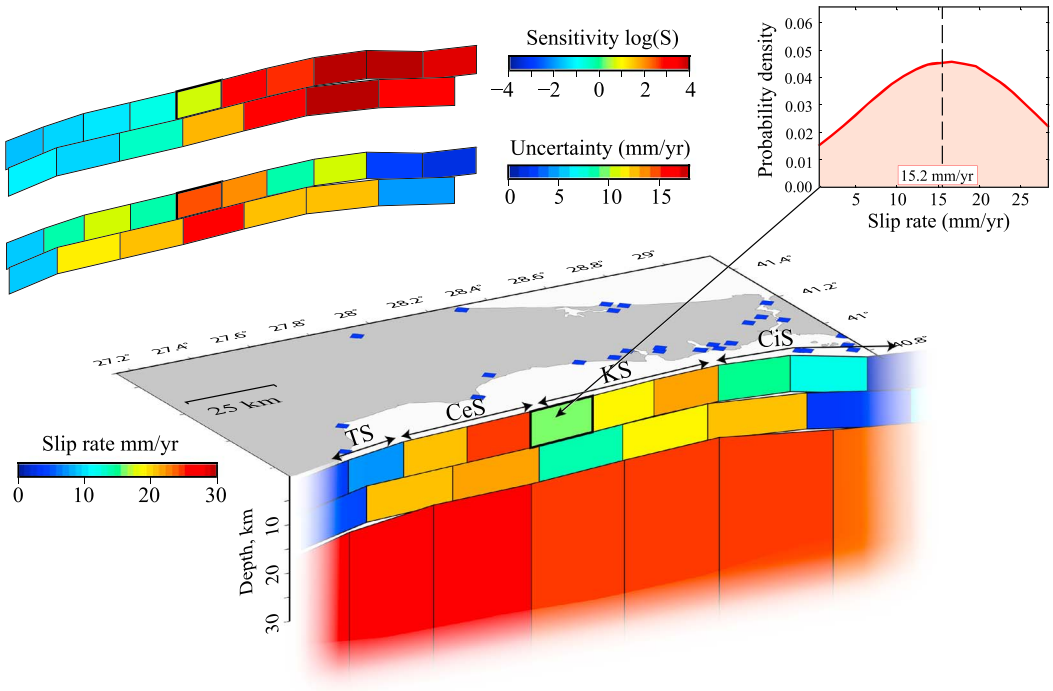

Figure 2. Posterior mean slip rate model (mm/yr). The top-left inset shows the slip sensitivity of the GPS network and the corresponding 2σ posterior uncertainties. The top-right inset shows the marginal PDF of interseismic slip rate in the KS (patch highlighted by thicker contour).

where $\mathbf{C}_\chi$ is the covariance matrix describing observational and prediction uncertainties [*Duputel et al.*, 2014] and $p(\mathbf{m})$ is the prior PDF of the model. To cope with the lack of realistic uncertainty estimates, we use a diagonal $\mathbf{C}_\chi$ whose elements correspond to residuals obtained after a first inversion (cf. Table S1 in the supporting information). The prior, $p(\mathbf{m})$, describes the information we have on model parameters before considering the data. We use simple uniform PDFs to ensure slip rate positivity in the right-lateral direction and uninformative broad uniform priors for geometrical transformation parameters. The prior for deep patches is defined as a narrow uniform PDF centered on 25 mm/yr [*McClusky et al.*, 2000; *Reilinger et al.*, 2006] (Figure S2).

Using such non-Gaussian definition of $p(\mathbf{m})$, there is no simple analytical form of $p(\mathbf{m}|\mathbf{d}_{obs})$. To evaluate the posterior PDF, we thus draw a large number of samples (i.e., ~300,000 models) from $p(\mathbf{m}|\mathbf{d}_{obs})$ using the parallel Monte Carlo approach described by *Minson et al.* [2013]. The final outcome is a posterior ensemble of plausible interseismic models that are consistent with both available GPS observations within errors and the prior assumptions described above. The posterior mean slip rate distribution is presented in Figure 2 with the associated 2σ uncertainties. Although this model cannot completely reproduce the variability of GPS velocity vectors north of the fault, the overall fit to the data is quite good (cf. Figure S3).

Our results indicate that the CiS and the Ganos fault are locked, which is consistent with previous studies [*Diao et al.*, 2016a; *Ergintav et al.*, 2014]. According to posterior uncertainty estimates (smaller than 5 mm/yr), this part of the model is well constrained. On the other hand, results suggest relatively large interseismic slip rate in the central segments (larger than 15 mm/yr in the TS and CeS). This is in agreement with the small slip deficit suggested by [*Ergintav et al.*, 2014] and the occurrence of strike-slip repeaters identified by [*Schmittbuhl et al.*, 2016], that may be associated with creep below 6 km. However, these portions of the model are associated with large uncertainties of the order of 10 mm/yr or larger. We also notice correlation of slip between neighbor patches in the CeS (Figure S4). This is probably due to the lack of GPS observations around the TS and CeS. To quantify our ability to detect slip in the seismogenic zone of the Marmara fault, we define the sensitivity of the GPS network as

$$S = \mathrm{diag}\left(\mathbf{G}^t \cdot \mathbf{C}_\chi^{-1} \cdot \mathbf{G}\right) \tag{3}$$

The results presented in the top left inset of Figure 2 clearly show that the current network is poorly sensitive to slip rate in the central part of the fault where our Bayesian analysis reveal large posterior uncertainties.

On the contrary, because of multiple GPS sites located on nearby islands, the sensitivity to slip in shallow portions of the CiS is larger. The Ganos fault is monitored only with a few sites, implying a small sensitivity to shallow slip for the entire geodetic network. However, these GPS stations are located close to the fault enabling good model resolution and small posterior uncertainties at shallow depth.

To improve our models, we need to upgrade the existing observational capability by designing a pertinent network enabling reliable measurements of strain accumulation in the Marmara region.

3. GPS Network Optimization

3.1. Network Optimization Procedure

Our aim is to evaluate where new GPS stations should be installed to optimize the resolution of shallow slip rate in the central part of the Marmara fault. The resolution on the fault is defined as [*Tarantola*, 2005]

$$R = \mathrm{diag}\left(C_m \cdot G^t \cdot \left(G \cdot C_m \cdot G^t + C_\chi\right)^{-1} \cdot G\right) \tag{4}$$

where C_m is the covariance matrix representing our prior information on the model while G and C_χ are the Green's functions and misfit covariance defined in equation (2). In this definition, the prior PDF on fault slip is a zero centered Gaussian of covariance C_m. We use a diagonal prior covariance with a standard deviation of 8.6 mm/yr, corresponding to the standard deviation of the uniform prior used in section 2.3 for the shallow patches.

To determine the optimum location of new stations, we use a global optimization procedure combining two different algorithms to maximize the minimum of resolution among a given set of subfaults [*Agram*, 2013]. First, we select stations improving the minimum resolution using a sequential algorithmic approach inspired from the subset selection algorithm of *Reeves and Zhe* [1999]. In a second step, site locations are optimized using the hybrid improvement algorithm [*Broughton et al.*, 2010], which enables the substitution of a previously selected station by a better candidate.

We design optimum GPS arrays using two different 3-D fault parameterizations of the seismogenic zone: (1) the simple two-row geometry previously used and (2) a more detailed geometry including three rows of subfaults. To ensure maximization of resolution at different depths in the seismogenic zone, we optimize the network independently for each row of subfaults. This optimization procedure is conducted only for the portion of the fault designated with a blue dashed line in Figures 3 and S5.

3.2. Terrestrial Network Optimization

We define a reference GPS network corresponding to existent sites (the same sites used for the Bayesian modeling), complemented by 15 sites that we installed in 2015. The set of additional candidate stations are distributed on a regular grid with 2 km spacing within 20 km of the coastline and 5 km spacing at larger distances. To avoid superposition of stations in the optimization procedure, we impose a minimum interstation distance of 5 km. Given the number of possible candidate GPS sites, our optimization algorithm evaluate the resolution matrix about half a million times. Resolution achieved for both tested geometries are presented in Figures 3 and S5, compared to the resolution estimated on the initial network. For the initial network (Figures 3a and S5a), the resolution of fault slip (R) in the CiS is already quite good. However, fault slip, it decreases drastically at depth and shows strong along-strike variations in the KS, CeS, and TS, even more visible using the more detailed geometry (Figure S5).

We first assume uniform uncertainties of 0.6 mm/yr for each new site corresponding to the observational error expected for survey sites measured regularly for at least 4 years. Graphs on Figures 3b and S5b show the evolution of minimum resolution achieved for each row of subfaults as more and more stations are added to the reference network. Note that the 15 survey sites installed in 2015 already enable some improvements of resolution. For both tested geometries, the resolution gain is relatively moderate (Figures 3a, 3b, S5a, and S5b) requiring a limited number of stations. To assess the effect of continuous stations instead of campaign sites, we also evaluate the fault slip resolution assuming observational uncertainties of 0.2 mm/yr for the previously optimized network. In this case, the resolution gain is significant, reaching 70% in the CeS, assuming the two-row geometry. Improvements are also important using the three-row geometry (Figure S5c), where the resolution in the first 10 km below surface is significantly larger. We have also tested the design of an optimized network assuming observational errors of 0.2 mm/yr. The resulting optimum site locations are nearly identical to the network optimization assuming 0.6 mm/yr (cf. Figure S6).

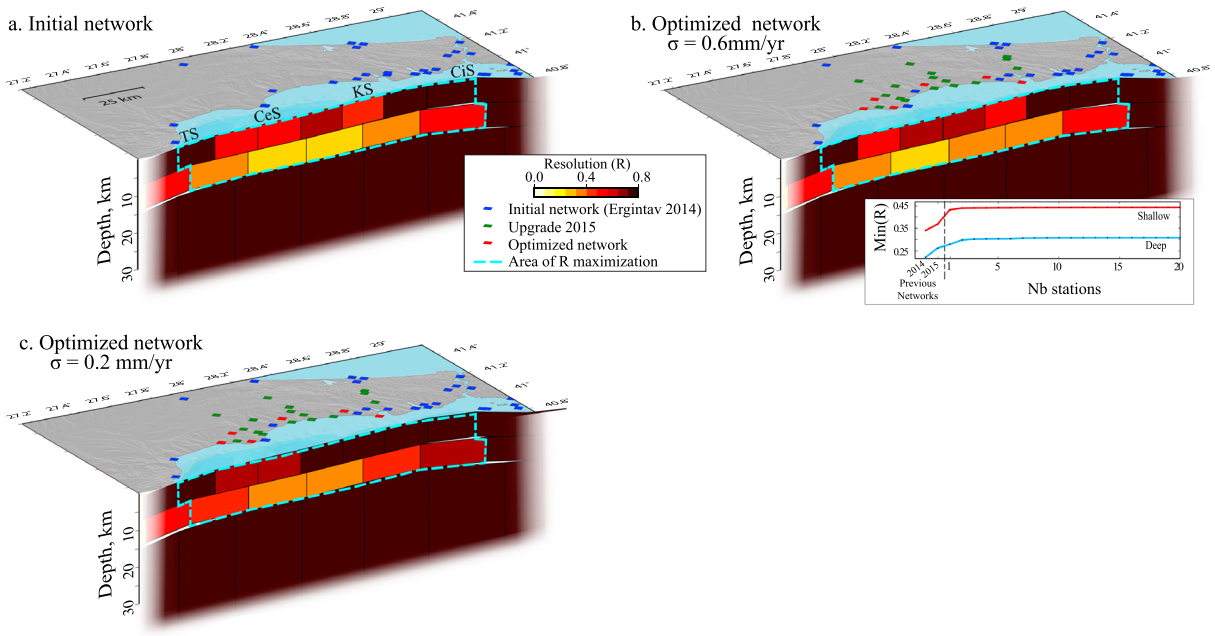

Figure 3. Model resolution of (a) the initial network; (b) the optimum network considering σ_d = 0.6 mm/yr; (c) the optimum network assuming σ_d = 0.2 mm/yr. The bottom right inset (Figure 3b) shows the minimum of resolution for each optimized row (area of maximization delimited by the dashed blue line) as function of the number of added stations.

For all tested configurations, adding stations on the coast of the TS is needed to maximize resolution at different depths. Other sites are also selected on the coast of the CeS and KS, especially on the peninsulas, where measurements can be made relatively close to the fault. The optimized networks with both fault geometries are relatively consistent. All optimum new sites are selected North of the fault. Candidate locations on the southern coast are too far away to bring additional information on the seismogenic zone. More sites are needed in the case of the three-row geometry, including a station selected on the Marmara Island, about 25 km south of the fault (cf. Figure S7).

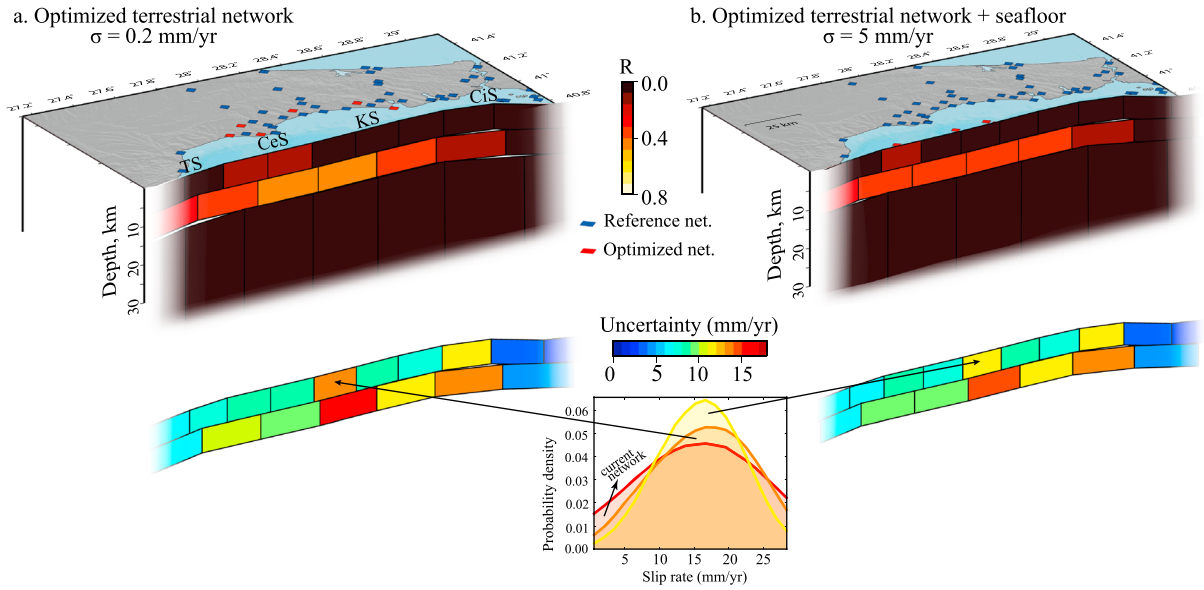

Figure 4. Model resolution compared to posterior 2σ uncertainties (bottom) on slip rate for (a) the terrestrial network (σ_d = 0.2 mm/yr); (b) the network combining onland (σ_d = 0.2 mm/yr) and seafloor sites (σ_d = 5 mm/yr). The bottom inset shows slip rate marginal PDFs for the current network (red; Figure 2), the optimum terrestrial network (orange), and the optimum network including onland and seafloor sites (yellow).

3.3. Seafloor Network Optimization

Seafloor measurements projects are now emerging to better capture interseismic strain accumulation. However, such measurements are currently limited to a small area and do not provide information about along-strike coupling variations on the NAF. To further improve the overall resolution of fault processes in the Marmara Sea, we investigate the possibility of adding seafloor measurement sites. In this case, the reference GPS network corresponds to existent sites, complemented by the 15 stations installed in 2015 and the optimum onland sites considering $\sigma = 0.2$ mm/yr (cf. section 3.2). Candidate seafloor sites are distributed on a regular grid with 2.5 km spacing, and a minimum interstation distance of 15 km is imposed. We assume uniform uncertainties of 5 mm/yr, according to previous estimates [e.g., *Yokota et al.*, 2016], albeit this value may be underestimated for such measurements. Six sites are selected very close to the fault in the KS and TS (Figure S7), where the coast is the furthest from the fault (Figure 4b). These sites are located on both sides of the fault trace and allow improvements of resolution on the central part of the Marmara fault. Resolution on deepest subfaults (between 7.5 km and 15 km depth) remains relatively small compared to shallow subfaults. We have added additional seafloor sites between the fault and the coast, but these stations have a very small effect on resolution due to their large observational errors. Nevertheless, our tests show that reducing uncertainty of seafloor measurements can improve resolution at larger depths (up to $R \sim 1$ assuming 1 mm/yr errors).

4. Discussions and Conclusion

We showed that 2-D fault modeling is not appropriate to evaluate strain accumulation on the Marmara fault. Indeed, simple tests assuming creeping or coupled segments result in deformation profiles that are quite different if we use an infinite strike-slip fault or a more realistic double-bend fault geometry. Beyond geometrical complexities, the Marmara fault can also present along-strike locking variations that cannot be inferred assuming an infinite linear strike-slip fault. Using a Bayesian approach, we generated probabilistic models of inter-seismic slip rate assuming a 3-D fault geometry. The posterior mean model is globally consistent with previous studies with locked segments in the Ganos fault and the CiS and aseismic creep on the central part of the Marmara fault [*Ergintav et al.*, 2014; *Diao et al.*, 2016a]. Going further, we have evaluated the probability distribution of moment deficit accumulated on the fault since previous large earthquakes (see supporting information). There is no significant slip deficit in the CeS (Figure S8), in agreement with the location of repeaters found by *Schmittbuhl et al.* [2016]. On the other hand, the KS and CiS are associated with significant moment deficits that are respectively sufficient to generate earthquakes of magnitude $M_w = 7.5 \pm 0.2$ and $M_w = 7.1 \pm 0.1$, in agreement with *Schmittbuhl et al.* [2015] (more details are provided in the supporting information).

Our analysis reveals large uncertainties of interseismic slip rate that complicate a more detailed interpretation of moment-rate deficit along the Marmara fault. Large posterior slip rate uncertainties presented in Figure 2 are mainly the result of poor data coverage in this region, which reduces the sensitivity of the GPS network to interseismic fault processes. These model uncertainties are also probably underestimated since we have neglected forward modeling errors assuming an homogeneous Earth model [*Duputel et al.*, 2014]. Future modeling studies based on larger data sets will have to account for the presence of a sedimentary cover [*Schmittbuhl et al.*, 2015] and possible deeper rigidity contrasts [*Le Pichon et al.*, 2005].

To improve future slip deficit estimates, we then pinpointed necessary improvements of the GPS network using a global optimization procedure. Using the results of this network design analysis, additional GPS sites have been installed during the 2016 summer to fill the gaps remaining after the first densification of the network in 2015. In the particular configuration of the Marmara Sea, where onland measurements are impossible within 20 km of the fault, our tests show that installing new survey sites will lead to relatively moderate improvements in the resolution of slip deficit (even if we add a large number of stations). In this context, the quality of measurements appears to be much more important than the quantity of measured sites. The installation of a limited number of permanent GPS stations can significantly and more rapidly help to assess fault coupling properties. These additional GPS stations must be installed as close as possible to the Marmara fault, on the coast of the TS, CeS, and KS (see Figures 3c and S5c). Even if adding a large number of observation points appears unnecessary, incorporating other data sets such as InSAR can be useful. Such additional observations bring redundant measurements over GPS data, thereby reducing observational uncertainties as $\sqrt{N_{\text{obs}}}$ (where N_{obs} is number of measurements at a given location).

To quantify the reduction of model uncertainties using different geodetic networks, we compare posterior slip rate uncertainties using the current network (Figure 2), the optimized terrestrial network and an optimum network with both onland and seafloor sites (cf. section 3 and Figure 4). Significant decreases of posterior uncertainties are already visible in the TS and KS segments considering the optimum terrestrial network only (cf. Figure 2 and Figure 4a). Largest uncertainties, of the order of 14 mm/yr in the CeS, can be reduced to about 10 mm/yr using seafloor measurements in the same region (Figure 4b). Although seafloor measurements are less efficient to improve the resolution at large depths (>7.5 km), such deployments are important to detect shallow creep (Figure 4b). Of course, the actual information gain depends on observational uncertainties and thus on the used seafloor measurements technology [*Sakic et al.*, 2016; *Yokota et al.*, 2016]. To attain sufficient resolution over the whole seismogenic zone, it is thus crucial to reduce seafloor measurement uncertainties.

The modeling of interseismic slip rate deficit depends on the tectonic setup and on the distribution of faults that are susceptible to break. Although we used a more accurate geometry than what was employed before, we do not take into account the spindle-shaped structure of the fault between the TS and CeS nor the South Marmara branch of the fault, less well defined in the bathymetry [*Le Pichon et al.*, 2001]. Nevertheless, *Schmittbuhl et al.* [2015] identified seismicity south of the CiS, which might indicate that the south Marmara fault is still active and potentially accumulating strain. Another issue is the possible occurrence of transient creep episodes separated by locking periods. Such behavior was already observed east of the Izmit and Düzce rupture zones where the shallow part of the NAF experienced a 1 month aseismic slip event in 2013 [*Rousset et al.*, 2016]. In the context of the Marmara Sea, such localized transient will be difficult to identify using only land-based geodetic measurements. Yet such aseismic events can play an important role in the overall strain accumulation budget of the fault.

Acknowledgments
This research was supported by the Initiative d'Excellence (IDEX) funding framework (Université de Strasbourg), the Institut National des Sciences de l'Univers (INSU ALEAS) and Hitit University Scientific Research Projects Fund (ODMYO19001.15.002). GPS data used in this study are published in *Ergintav et al.* [2014]. We thank Romain Jolivet, Jean Schmittbuhl, Olivier Lengliné and Emanuela Matrullo for helpful discussions and Mark Simons for providing some of the codes used in this study. Finally, we thank the editor A. Newman and two anonymous reviewers for their constructive comments, which helped to improve this manuscript.

References

Agram, P. S. (2013), *Post-Doctoral Fellowship Report*, Caltech Keck Institute for Space Studies, Pasadena, Calif.
Aktug, B., A. Dogru, H. Ozener, and M. Peyret (2015), Slip rates and locking depth variation along central and easternmost segments of North Anatolian Fault, *Geophys. J. Int.*, *202*, 2133–2149, doi:10.1093/gji/ggv274.
Ambraseys, N. (2002), The seismic activity of the Marmara Sea region over the last 2000 years, *Bull. Seismol. Soc. Am.*, *92*(1), 1–18.
Armijo, R., et al. (2005), Submarine fault scarps in the sea of Marmara pull-apart (North Anatolian Fault): Implications for seismic hazard in Istanbul, *Geochem. Geophys. Geosyst.*, *6*, Q06009, doi:10.1029/2004GC000896.
Barbot, S., P. Agram, and M. De Michele (2013), Change of apparent segmentation of the San Andreas fault around Parkfield from space geodetic observations across multiple periods, *J. Geophys. Res. Solid Earth*, *118*, 6311–6327, doi:10.1002/2013JB010442.
Bohnhoff, M., P. Martínez-Garzón, F. Bulut, E. Stierle, and Y. Ben-Zion (2016), Maximum earthquake magnitudes along different sections of the North Anatolian Fault zone, *Tectonophysics*, *674*, 147–165, doi:10.1016/j.tecto.2016.02.028.
Broughton, R., I. Coope, P. Renaud, and R. Tappenden (2010), Determinant and exchange algorithms for observation subset selection, *IEEE Trans. Image Process.*, *19*(9), 2437–2443.
Bürgmann, R., S. Ergintav, P. Segall, E. H. Hearn, S. McClusky, R. E. Reilinger, H. Woith, and J. Zschau (2002), Time-dependent distributed afterslip on and deep below the Izmit earthquake rupture, *Bull. Seismol. Soc. Am.*, *92*(1), 126–137.
Diao, F., T. Walter, G. Solaro, R. Wang, M. Bonano, M. Manzo, S. Ergintav, Y. Zheng, X. Xiong, and R. Lanari (2016a), Fault locking near Istanbul: Indication of earthquake potential from InSAR and GPS observations, *Geophys. J. Int.*, *205*(1), 490–498.
Diao, F., R. Wang, H. Aochi, T. R. Walter, Y. Zhang, Y. Zheng, and X. Xiong (2016b), Rapid kinematic finite-fault inversion for an M_w 7+ scenario earthquake in the Marmara Sea: An uncertainty study, *Geophys. J. Int.*, *204*(2), 813–824.
Duputel, Z., P. S. Agram, M. Simons, S. E. Minson, and J. L. Beck (2014), Accounting for prediction uncertainty when inferring subsurface fault slip, *Geophys. J. Int.*, *197*(1), 464–482.
Ergintav, S., R. Bürgmann, S. McClusky, R. Cakmak, R. Reilinger, O. Lenk, A. Barka, and H. Özener (2002), Postseismic deformation near the Izmit earthquake (17 August 1999, M 7.5) rupture zone, *Bull. Seismol. Soc. Am.*, *92*(1), 194–207.
Ergintav, S., R. Reilinger, R. Çakmak, M. Floyd, Z. Cakir, U. Doğan, R. King, S. McClusky, and H. Özener (2014), Istanbul's earthquake hot spots: Geodetic constraints on strain accumulation along faults in the Marmara seismic gap, *Geophys. Res. Lett.*, *41*, 5783–5788, doi:10.1002/2014GL060985.
Hearn, E., S. McClusky, S. Ergintav, and R. Reilinger (2009), Izmit earthquake postseismic deformation and dynamics of the North Anatolian Fault zone, *J. Geophys. Res.*, *114*, B08405, doi:10.1029/2008JB006026.
Hussain, E., A. Hooper, T. J. Wright, R. J. Walters, and D. P. S. Bekaert (2016), Interseismic strain accumulation across the central North Anatolian Fault from iteratively unwrapped InSAR measurements, *J. Geophys. Res. Solid Earth*, *121*, 9000–9019, doi:10.1002/2016JB013108.
Jolivet, R., M. Simons, P. Agram, Z. Duputel, and Z.-K. Shen (2015), Aseismic slip and seismogenic coupling along the central San Andreas fault, *Geophys. Res. Lett.*, *42*, 297–306, doi:10.1002/2014GL062222.
Le Pichon, X., et al. (2001), The active main Marmara fault, *Earth Planet. Sci. Lett.*, *192*(4), 595–616.
Le Pichon, X., N. Chamot-Rooke, C. Rangin, and A. Sengör (2003), The North Anatolian Fault in the Sea of Marmara, *J. Geophys. Res.*, *108*(B4), 2179, doi:10.1029/2002JB001862.
Le Pichon, X., C. Kreemer, and N. Chamot-Rooke (2005), Asymmetry in elastic properties and the evolution of large continental strike-slip faults, *J. Geophys. Res.*, *110*, B03405, doi:10.1029/2004JB003343.
Maurer, J., and K. Johnson (2014), Fault coupling and potential for earthquakes on the creeping section of the central San Andreas fault, *J. Geophys. Res. Solid Earth*, *119*, 4414–4428, doi:10.1002/2013JB010741.
McClusky, S., et al. (2000), Global Positioning System constraints on plate kinematics and dynamics in the eastern Mediterranean and Caucasus, *J. Geophys. Res.*, *105*(B3), 5695–5719.

Meghraoui, M., M. E. Aksoy, H. S. Akyüz, M. Ferry, A. Dikbaş, and E. Altunel (2012), Paleoseismology of the North Anatolian Fault at Güzelköy (Ganos segment, Turkey): Size and recurrence time of earthquake ruptures west of the Sea of Marmara, *Geochem. Geophys. Geosyst.*, *13*, Q04005, doi:10.1029/2011GC003960.

Minson, S., M. Simons, and J. Beck (2013), Bayesian inversion for finite fault earthquake source models I—Theory and algorithm, *Geophys. J. Int.*, *194*(3), 1701–1726.

Okada, Y. (1985), Surface deformation due to shear and tensile faults in a half-space, *Bull. Seismol. Soc. Am.*, *75*(4), 1135–1154.

Reeves, S. J., and Z. Zhe (1999), Sequential algorithms for observation selection, *IEEE Trans. Signal Process.*, *47*(1), 123–132.

Reilinger, R., et al. (2006), GPS constraints on continental deformation in the Africa-Arabia-Eurasia continental collision zone and implications for the dynamics of plate interactions, *J. Geophys. Res.*, *111*, B05411, doi:10.1029/2005JB004051.

Rousset, B., R. Jolivet, M. Simons, C. Lasserre, B. Riel, P. Milillo, Z. Çakir, and F. Renard (2016), An aseismic slip transient on the North Anatolian Fault, *Geophys. Res. Lett.*, *43*, 3254–3262, doi:10.1002/2016GL068250.

Sakic, P., et al. (2016), No significant steady state surface creep along the North Anatolian Fault offshore Istanbul: Results of 6 months of seafloor acoustic ranging, *Geophys. Res. Lett.*, *43*(13), 6817–6825.

Savage, J., and R. Burford (1973), Geodetic determination of relative plate motion in central California, *J. Geophys. Res.*, *78*(5), 832–845.

Schmittbuhl, J., H. Karabulut, O. Lengliné, and M. Bouchon (2015), Seismicity distribution and locking depth along the main Marmara fault, Turkey, *Geochem. Geophys. Geosyst.*, *17*, 954–965, doi:10.1002/2015GC006120.

Schmittbuhl, J., H. Karabulut, O. Lengliné, and M. Bouchon (2016), Long-lasting seismic repeaters in the central basin of the main Marmara fault, *Geophys. Res. Lett.*, *43*, 9527–9534, doi:10.1002/2016GL070505.

Stein, R. S., A. A. Barka, and J. H. Dieterich (1997), Progressive failure on the North Anatolian Fault since 1939 by earthquake stress triggering, *Geophys. J. Int.*, *128*(3), 594–604.

Straub, C., H.-G. Kahle, and C. Schindler (1997), GPS and geologic estimates of the tectonic activity in the Marmara Sea region, NW Anatolia, *J. Geophys. Res.*, *102*(B12), 27,587–27,601.

Tarantola, A. (2005), *Inverse Problem Theory and Methods for Model Parameter Estimation*, SIAM, Philadelphia, Pa.

Tatar, O., et al. (2012), Crustal deformation and kinematics of the eastern part of the North Anatolian Fault zone (Turkey) from {GPS} measurements, *Tectonophysics*, *518-521*, 55–62, doi:10.1016/j.tecto.2011.11.010.

Yokota, Y., T. Ishikawa, S.-I. Watanabe, T. Tashiro, and A. Asada (2016), Seafloor geodetic constraints on interplate coupling of the Nankai trough megathrust zone, *Nature*, *534*, 374–377.